nature nanotechnology

ARTICLES

https://doi.org/10.1038/s41565-021-00869-5

Check for updates

# Ultra-high-frequency radio-frequency acoustic molecular imaging with saline nanodroplets in living subjects

Yun-Sheng Chen[1,2]✉, Yang Zhao[2,3], Corinne Beinat[1], Aimen Zlitni[1], En-Chi Hsu[1], Dong-Hua Chen[4], Friso Achterberg[1], Hanwei Wang[2], Tanya Stoyanova[5], Jennifer Dionne[3] and Sanjiv Sam Gambhir[1,3,5,6,7]

**Molecular imaging is a crucial technique in clinical diagnostics but it relies on radioactive tracers or strong magnetic fields that are unsuitable for many patients, particularly infants and pregnant women. Ultra-high-frequency radio-frequency acoustic (UHF-RF-acoustic) imaging using non-ionizing RF pulses allows deep-tissue imaging with sub-millimetre spatial resolution. However, lack of biocompatible and targetable contrast agents has prevented the successful in vivo application of UHF-RF-acoustic imaging. Here we report our development of targetable nanodroplets for UHF-RF-acoustic molecular imaging of cancers. We synthesize all-liquid nanodroplets containing hypertonic saline that are stable for at least 2 weeks and can produce high-intensity UHF-RF-acoustic signals. Compared with concentration-matched iron oxide nanoparticles, our nanodroplets produce at least 1,600 times higher UHF-RF-acoustic signals at the same imaging depth. We demonstrate in vivo imaging using the targeted nanodroplets in a prostate cancer xenograft mouse model expressing gastrin release protein receptor (GRPR), and show that targeting specificity is increased by more than 2-fold compared with untargeted nanodroplets or prostate cancer cells not expressing this receptor.**

Early cancer diagnosis remains one of the main aims in clinical oncology since it has been shown to greatly improve treatment effectiveness and disease containment[1]. To detect cancers non-invasively at an early stage, high sensitivity, high spatial resolution and large imaging depth are often needed simultaneously[2,3]. Unfortunately, enhancing one of these capabilities often leads to trade-offs with the others. For example, positron emission tomography (PET) and single-photon emission computed tomography (SPECT) offer high sensitivity with infinite imaging depth but provide moderate imaging resolution. Computed tomography (CT) and magnetic resonance imaging (MRI) provide millimetre spatial resolution with relatively low molecular sensitivity[3–7]. Moreover, PET, SPECT and CT all use ionizing radiation and are not a suitable choice for patients vulnerable to radiation exposure[8]. Molecular ultrasound imaging uses non-ionizing sound waves and provides high spatial resolution down to micrometres, but the large size of imaging agents (microbubbles) suffers from non-extravasation to the tumour site[9,10]. Several nanosized ultrasound imaging agents, such as acoustic nanodroplets, have been developed recently[11]. However, they usually require an external ultrasound burst to vaporize the nanodroplets to microbubbles, and thus may limit the targets to where the proximal positions are known[11]. On the other hand, molecular photoacoustic imaging accommodates extravasated contrast agents, but typically penetrates to depths of less than 3 cm in tissue due to strong attenuation of light[12]. Therefore, developing new non-ionizing molecular imaging techniques that offer imaging at high depths and spatial resolution with high sensitivity remains an outstanding challenge.

Radio-frequency acoustic (RF-acoustic) imaging is an emerging technique that generates ultrasound images by illuminating tissue with non-ionizing electromagnetic pulses in the frequency range of 20 kHz–300 GHz (Fig. 1a)[13–19]. In tissue, electromagnetic waves decay with depth due to absorption and scattering, where the decay rate is frequency dependent. RF waves in the ultra-high-frequency (UHF) band (300 MHz–1 GHz) decay 100 times slower with depth than light, and 10 times slower than microwave (1 GHz–300 GHz)[20]. Thus, UHF-RF-acoustic imaging (Fig. 1b) can potentially image much deeper than optical, photoacoustic or microwave-acoustic imaging techniques (see 'Comparisons of UHF-RF-acoustic imaging with other acoustic-based imaging' in Supplementary Information)[19,21]. In addition, differences in RF absorption between cancerous and normal tissue in the UHF range have been reported, suggesting that UHF-RF-acoustic imaging can potentially differentiate cancerous tissue from healthy tissue[11,12]. However, due to the limited choices of biocompatible UHF-RF-absorbing materials to date, the application of UHF-RF-acoustic molecular imaging using exogenous contrast agents in vivo has not been reported. In this work, we report the development and thorough evaluation of a stable liquid UHF-RF-acoustic nanoparticle, and its utility for molecular imaging of prostate cancer.

## Design concept for achieving UHF-RF-acoustic contrast

In UHF, the dominant heating mechanism is Joule heating caused by collision of charged carriers[20]. Ideal choices for UHF-RF-acoustic contrast agents are materials that either have high dielectric loss

[1]Department of Radiology, Molecular Imaging Program at Stanford (MIPS), Stanford University School of Medicine, Stanford, CA, USA. [2]Department of Electrical and Computer Engineering, University of Illinois at Urbana-Champaign, Urbana, IL, USA. [3]Department of Materials Science and Engineering, Stanford University, Stanford, CA, USA. [4]Department of Structural Biology, Stanford University, Stanford, CA, USA. [5]Canary Center at Stanford for Cancer Early Detection, Stanford University, Stanford, CA, USA. [6]Department of Bioengineering, Stanford University, Stanford, CA, USA. [7]Deceased to Sanjiv Sam Gambhir
✉e-mail: yunsheng@illinois.edu

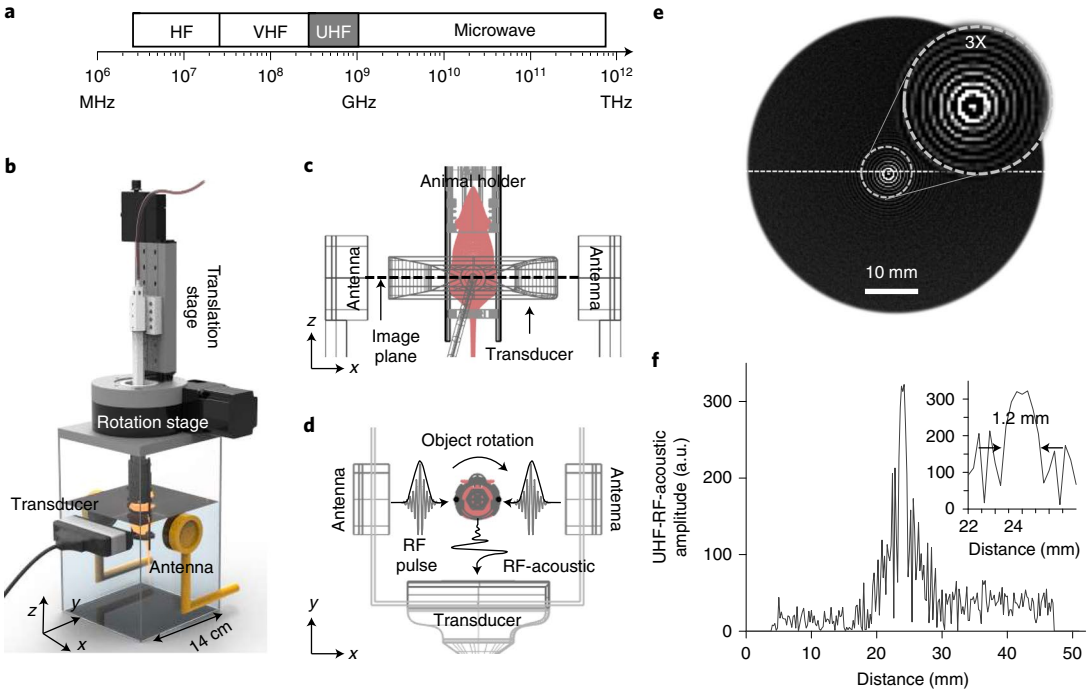


**Fig. 1 | Experimental concept. a**, The spectral range of electromagnetic waves in the RF range, where the UHF band ranges from 300 MHz to 1 GHz. **b**, Perspective view of the experimental setup for UHF-RF-acoustic imaging of mice. The acoustic transducer is mounted on the side to image the *x*–*y* plane. The mouse is mounted vertically along the *z* axis. A translational stage can move the mouse in the ±*z* direction and the rotational stage rotates the mouse in the *x*–*y* plane. Two RF antennae emit RF pulses (160 ns) to excite the UHF-RF-acoustic signals. The same setup was also used for scanning tissue phantoms. **c**, The side view (*x*–*z* plane) of the experimental setup. **d**, The top view (*x*–*y* plane) of the experimental setup. **e**, Point spread function of the UHF-RF-acoustic system; the enlarged view shows the UHF-RF-acoustic signal pattern generated with a point source. **f**, One-dimensional point spread function of the UHF-RF-acoustic system. The inset shows the full width at half-maximum is 1.2 mm.

or conductivity at the frequency of interest (300 MHz–1 GHz)[20,22]. While several types of nanoparticles, including gold, silicon, carbon nanotubes and iron oxide ($Fe_3O_4$) nanoparticles, have been investigated for RF-acoustic imaging, these particles showed weak RF-acoustic signals in the UHF range[20,22–24]. On the other hand, liquid electrolytes with high ionic conductivity, such as aqueous salt solutions, produce much stronger UHF-RF-acoustic signals, making them ideal choices for developing UHF-RF-acoustic contrast agents[22,25]. To determine the ideal salt solution, five candidates, NaCl(aq.), KI(aq.), KCl(aq.), $MgCl_2$(aq.) and $CaCl_2$(aq.), were assessed for their ionic conductivity, solubility in water, biocompatibility and UHF-RF-acoustic signals. In addition, NaOH(aq.), despite its toxicity, was also used as a positive control due to its known high ionic conductivity. The UHF-RF-acoustic signals were measured using a prototype RF-acoustic tomography system (see 'UHF-RF-acoustic imaging system' in Supplementary Information) with nanosecond UHF-RF pulses at 433 MHz frequency, which is within the medical device radiocommunications service band (Fig. 1).

As expected, Fig. 2b shows that NaOH(aq.) (4 wt%, to avoid signal saturation) produces the strongest UHF-RF-acoustic signal, followed by KCl(aq.) and NaCl(aq.) (both 10 wt%). Interestingly, a linear correlation between the UHF-RF-acoustic amplitude of these electrolyte solutions and their conductivity was found ($R^2 = 0.92$), confirming that the UHF-RF-acoustic signals are mainly related to the conductivity and minimally associated with the type of salt (Fig. 2c).

Because saline is known to have the highest electrical conductivity among these salts at its saturated concentration (~25 wt%)[26,27], we decided to further investigate its potential as an UHF-RF-acoustic contrast agent.

To provide molecular information using UHF-RF-acoustic imaging, the contrast agent needs to be targeted to a specific marker of disease. Unfortunately, salts in water consist of ions which easily diffuse away in tissue and cannot be functionalized to molecular targeting ligands, such as antibodies and peptides. Hence, saline needs to be first encapsulated into a stable nanoparticle for subsequent conjugation with molecularly targeted ligands. Many approaches using hydrophobic biomaterials (such as lipids and biodegradable polymers) to encapsulate aqueous nanodroplets (also called double emulsions or water/oil/water emulsions) have been used in medicine[28,29], cosmetics and the food industry[30,31], and in imaging[32,33]. Unfortunately, none of these existing nanodroplets can stably sustain the large outward osmotic pressure caused by the differential ionic concentrations between the core and outer aqueous solutions[34,35]. Such stability, however, is essential for producing reliable imaging signals for medical imaging applications.

Previous theoretical studies showed that altering the solute and water permeability of the oil phase greatly affects the size of the nanodroplets[36], suggesting that reducing water permeability in the oil phase can greatly reduce its swelling[36–38]. Macroscopically, water permeability is directly related to bulk water solubility of the material. After reviewing water solubility in various biocompatible liquids[35,39,40], perfluorocarbon liquids were chosen for our nanoparticle formulation due to their notably lower water solubility and frequent utility in various biomedical applications[41]. Perfluorocarbon liquids, including perfluoropentane[42], perfluorohexane[42], perfluoro-15-crown-5-ether[42] and perfluorodecalin[43], were evaluated to determine the optimum shell to stabilize our saline droplets. In addition, soybean oil[44], a commonly used hydrocarbon liquid, was used as a reference 'oil phase'.

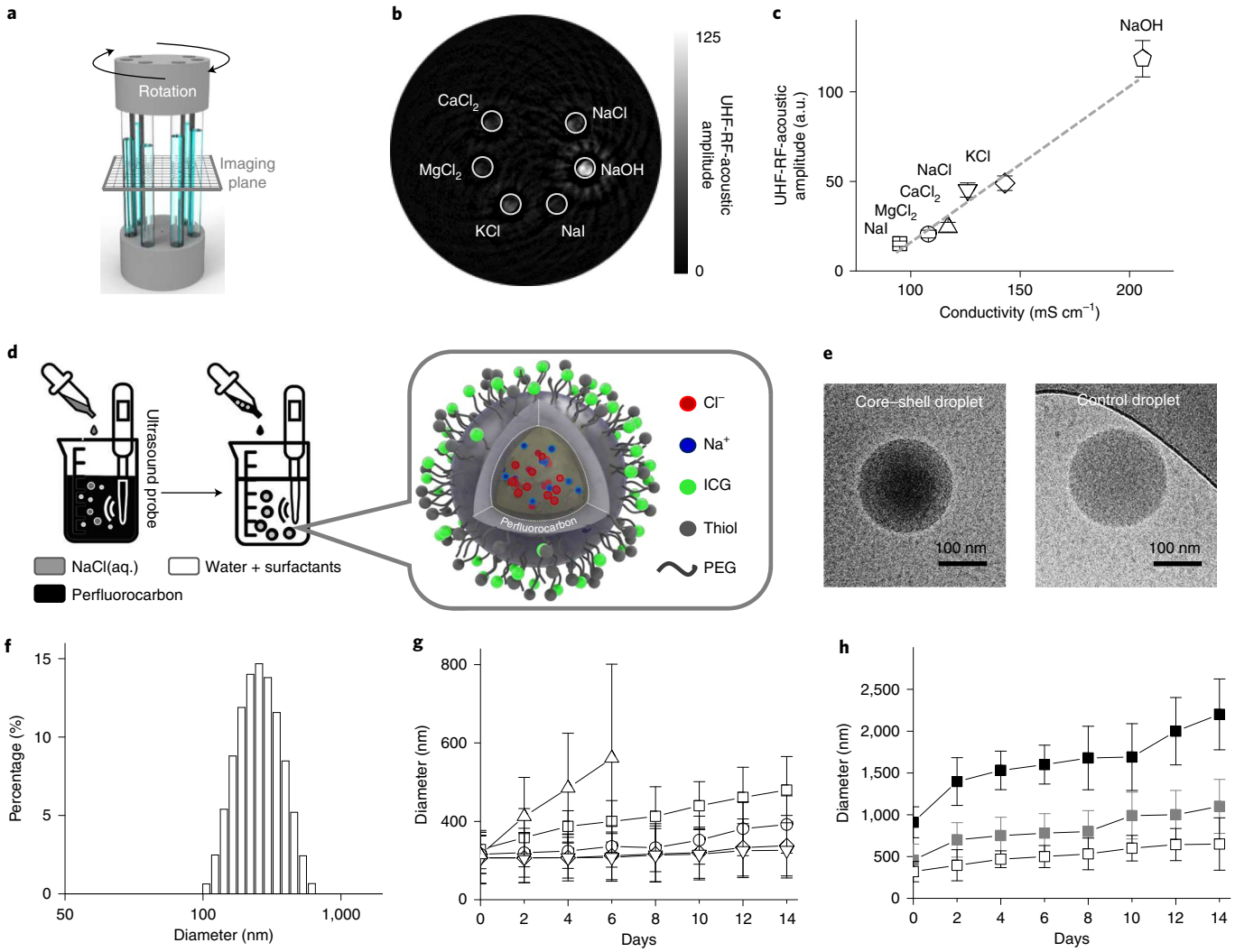


**Fig. 2 | Preparation of UHF-RF-acoustic contrast agents with engineered saline nanodroplets. a**, Experimental setup of the tube phantom for in vitro imaging with each tube containing different concentrations of electrolytes. **b**, UHF-RF-acoustic images of various types of electrolytes; the 1-mm-diameter tubes contain 10 wt% of NaCl, NaI, KCl, $MgCl_2$ and $CaCl_2$, and 4 wt% of NaOH. **c**, UHF-RF-acoustic signal amplitude as a function of conductivity of the abovementioned electrolytes. The generated UHF-RF-acoustic peak amplitude follows a linear trend with the conductivity (grey dotted lines, $R^2 = 0.92$). Data are presented as mean values ± s.d. ($n = 5$). **d**, A schematic illustration of nanodroplet synthesis using the double-emulsion approach. **e**, Cryo-electron microscopy images showing nanodroplets with NaCl(aq.) (25 wt%) core and perfluorocarbon shell (left) and a control droplet with only perfluorocarbon (right). **f**, Measured size distribution of the nanodroplets using dynamic light scattering, showing an average diameter of the nanodroplets ~250 nm. **g**, Stability test of nanodroplets with a median diameter of 250 nm with various shells, including soybean oil (control, triangle), perfluoropentane (square), perfluorohexane (circle), perfluoro-15-crown-5-ether (rhombus) and perfluorodecalin (inverted triangle). Data are presented as mean values ± s.d. ($n = 25$). By day 6, the soybean oil nanodroplets increase in size by ~215% relative to day 0 ($P < 0.0001$). By day 14, the diameters of nanodroplets with perfluorodecalin, perfluoro-15-crown-5-ether, perfluorohexane and perfluoropentane shells increased by 18 ± 15% ($P = 0.2273$), 28 ± 17% ($P = 0.0751$), 65 ± 17% ($P < 0.0001$) and 103 ± 18% ($P < 0.0001$). **h**, Stability test of nanodroplets with perfluoropentane shell with average diameters of 250 nm (open square), 450 nm (grey solid square) and 800 nm (black solid square); by day 14, the 250 nm nanodroplets had increased by 103 ± 18% ($P < 0.0001$), the 450 nm by 139 ± 18% ($P < 0.0001$) and the 800 nm by 142 ± 20% ($P < 0.0001$). Data are presented as mean values ± s.d. ($n = 25$).

## Synthesis and stability characterization of saline nanodroplets

A double-emulsion method was developed to encapsulate hypertonic saline (up to 25 wt%) inside the nanoparticles (Fig. 2d and 'Synthesis of nanodroplets' in Supplementary Information). To confirm saline encapsulation, the double-emulsion nanodroplets were compared with the single-phase perfluorohexane nanodroplets by cryo-electron microscopy. Figure 2e shows the differential contrasts inside the double emulsion, confirming the core–shell configuration (left panel), whereas uniform contrast of the single-phase nanodroplets was observed (right panel). In addition, we were able to control the size of the nanodroplets and produce uniform particles (polydispersity <0.1) by adjusting the ultrasound power and the pore size of the extrusion filter (Fig. 2f and Supplementary Fig. 2).

The stability of the nanodroplets was monitored for 2 weeks by assessing changes in size through dynamic light scattering (DLS) analysis. Figure 2g shows that the soybean oil nanodroplets more than doubled in size (~215%) after only 6 days, whereas negligible changes in the perfluorocarbon nanodroplets were observed. After 6 days, due to the large polydispersity of the soybean oil nanodroplets, we could no longer measure their sizes using DLS, while the size of perfluorocarbon nanodroplets remained stable for

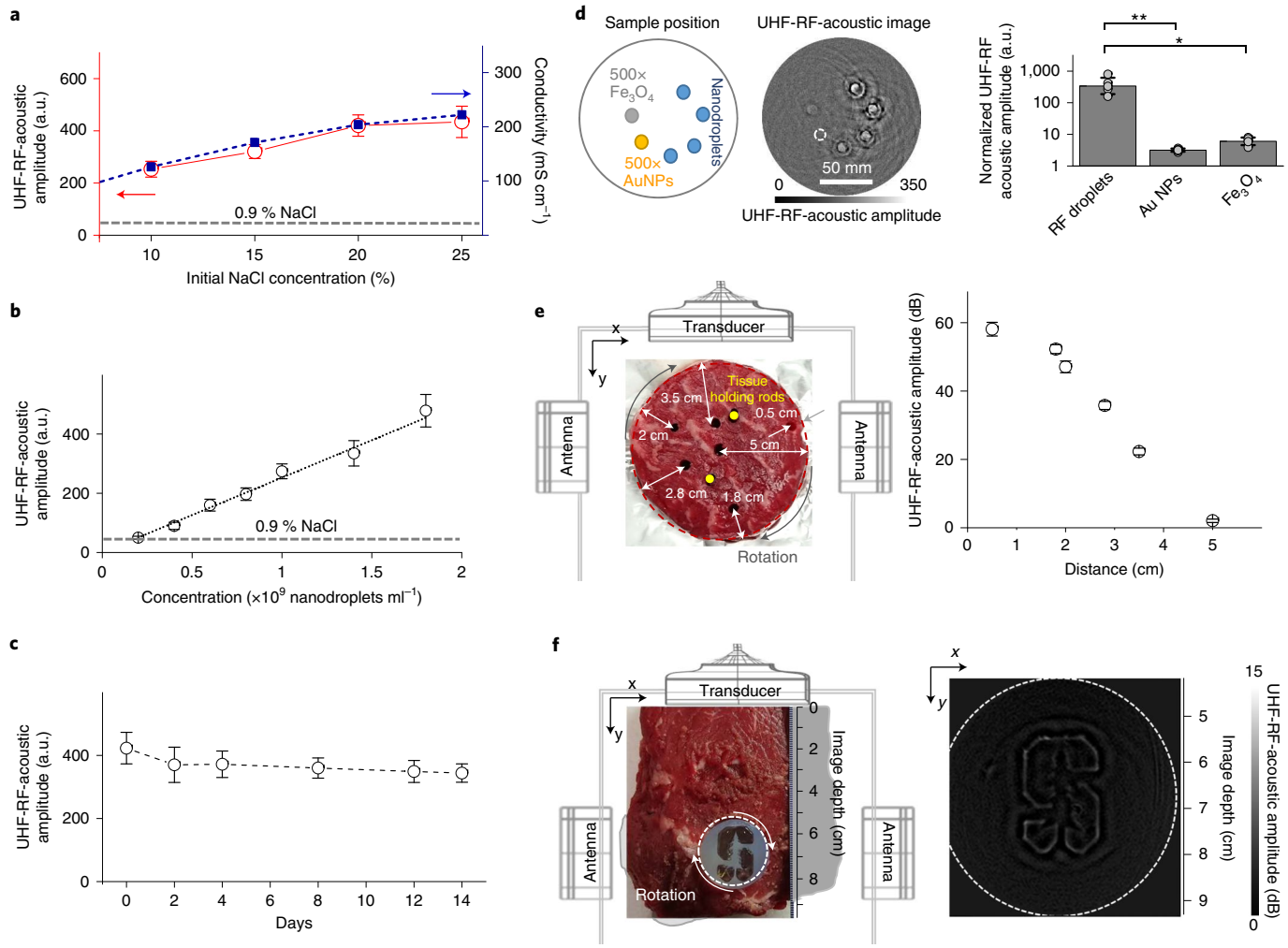


**Fig. 3 | In vitro contrast-enhanced UHF-RF-acoustic imaging. a**, UHF-RF-acoustic signal amplitude of saline nanodroplets (red open circles) versus the initial concentration of NaCl(aq.), and the corresponding conductivity (blue solid squares, conductivity data adapted from ref. [27]). Data are presented as mean values ± s.d. ($n=5$). **b**, UHF-RF-acoustic signal amplitude versus nanodroplet concentration with encapsulated 25 wt% saline, showing a linear correlation ($R^2=0.995$). Data are presented as mean values ± s.d. ($n=5$). The grey dashed line shows the UHF-RF-acoustic signal level of physiological saline (0.9 wt%). **c**, UHF-RF-acoustic signal amplitude versus ageing time over 14 days. Nanodroplets ($1.8\times10^9$ nanodroplets ml$^{-1}$) containing 25 wt% saline were measured; data are presented as mean values ± s.d. ($n=5$). **d**, UHF-RF-acoustic signal amplitude of 1-mm-diameter tube phantoms. Six tubes were imaged: four tubes contain nanodroplets ($1\times10^9$ nanodroplets ml$^{-1}$); one contains 20 nm gold nanoparticles (AuNPs, $5\times10^{11}$ nanoparticles ml$^{-1}$); and one contains 100 nm $Fe_3O_4$ nanoparticles ($5\times10^{11}$ nanoparticles ml$^{-1}$). Both AuNPs and $Fe_3O_4$ nanoparticles were prepared at 500× higher concentration than the nanodroplets to bring their UHF-RF-acoustic signals above the noise level. The 1× nanodroplets produce 3.2 ± 0.7 times higher UHF-RF-acoustic signals than the 500× $Fe_3O_4$ nanoparticles (*$P=0.0002$, $n=5$), and 5.1 ± 0.6 times higher signals than the 500× AuNPs (**$P=1.4\times10^{-7}$, $n=5$). Data are presented as mean values ± s.d. **e**, UHF-RF-acoustic signal amplitude of nanodroplets as a function of imaging depth in bovine tissue (photograph with setup on the left). Six 3-mm-diameter inclusions were imaged, located at 0.5, 1.8, 2, 2.8, 3.5 and 5 cm from the tissue surface. Each inclusion contains 1:1 volume ratio of nanodroplets ($3\times10^9$ nanoparticles ml$^{-1}$ with 25 wt% saline) and 12% gelatin. Data are presented as mean values ± s.d. ($n=5$). **f**, UHF-RF-acoustic imaging of a Stanford logo phantom. The phantom contains nanodroplets ($8\times10^9$ nanodroplets ml$^{-1}$); the inclusion rotates for tomographic imaging.

up to 14 days. Specifically, the increases in diameters of perfluorodecalin, perfluoro-15-crown-5-ether, perfluorohexane and perfluoropentane nanodroplets were 18 ± 15%, 28 ± 17%, 65 ± 17% and 103 ± 18% after 14 days, respectively. These results indicate the importance of the utilized perfluorocarbon liquids and their effects on nanodroplet stability.

It is known that the stability of perfluorocarbon nanodroplets is strongly related to the molecular diffusivity of the perfluorocarbons, which is greatly affected by the molecular weight and the structure of the perfluorocarbon molecules[45]. Typically, a decrease in molecular diffusivity results in a decrease in water solubility, an increase in interfacial tension and a slowing of the rate of Ostwald ripening, and ultimately an increase in the emulsion stability[38,46]. In the nanodroplets (double emulsions), the diffusivities could also affect the rates of inward water permeability and hence stability. The different types of perfluorocarbon nanodroplets have different shelf-lives in our stability study, probably due to their differences in molecular diffusivity (Fig. 2g). Although it is non-trivial to directly measure the molecular diffusivities of the perfluorocarbon molecules in nanodroplets, a strong relation between the molecular diffusivity and the vapour pressure has been previously demonstrated[38]. Specifically, high-vapour-pressure liquid has a high molecular diffusivity because of the weak interactions between molecules[47]; therefore, the vapour pressure of each perfluorocarbon liquid is a more predictive factor than molecular diffusivity to test the stability of nanodroplets. Figure 2g and Supplementary Table 2

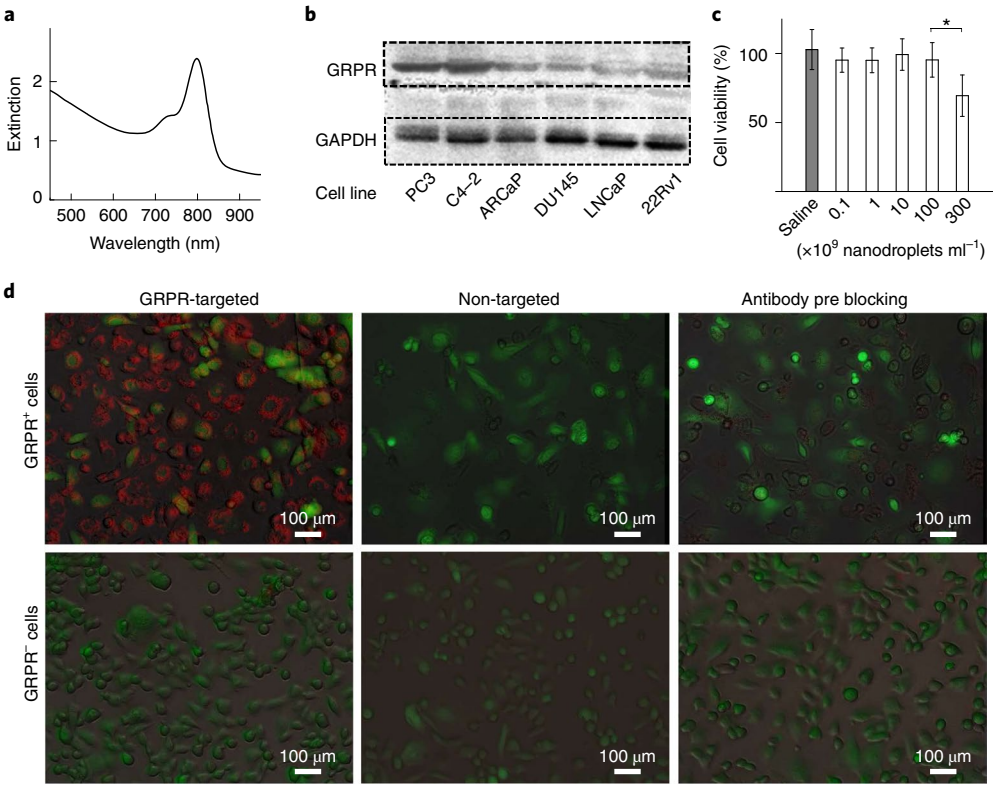


**Fig. 4 | GRPR-targeted nanodroplets showed specific targeting to prostate cancer cells and low toxicity in cell culture. a**, Extinction spectrum of the nanodroplets shows the optical absorption peak from ICG dye. **b**, Western blot analysis for GRPR expression in different prostate cancer cell lines. **c**, Cell viability test using non-targeted nanodroplets, showing no obvious reduction in cell viability when cells were incubated with up to $1\times10^{11}$ nanodroplets ml$^{-1}$ ($P=0.958$ relative to control), and low cell toxicity up to $3\times10^{11}$ nanodroplets ml$^{-1}$ (*$P=0.009$, $n=30$) at 24 h postincubation relative to cells incubated in the absence of nanodroplets. Data are presented as mean values ± s.d. ($n=30$). **d**, Optical fluorescence imaging of ICG-labelled targeted (column 1) and non-targeted (column 2) nanodroplets incubated with GRPR$^+$ (PC3) and GRPR$^-$ (DU145) cells at 12 h postincubation. Column 3 shows the optical fluorescence imaging of ICG-labelled targeted nanodroplets incubated with antibody-preblocked PC3 and DU145 cells, also at 12 h postincubation. Both PC3 and DU145 cells express green fluorescent protein (GFP). ICG dyes on nanodroplets and GFP on the cells are shown as red and green, respectively.

show how the size expansion of nanodroplets decreases as the vapour pressure of perfluorocarbon liquids decreases.

To further examine what other factors affect the stability, we chose the same type of perfluorocarbon nanodroplets but changed their sizes. When the surfactants and surrounding solvent are the same, it is known that the effective boiling point of perfluorocarbon liquid in the emulsion is mainly affected by the size-dependent Laplace pressure, which is a work balance between tension and applied pressure at the curved interface of particles[42,47,48]. When the size of nanodroplets decreases, Laplace pressure increases and leads to a high effective boiling temperature. Similar effects have been demonstrated in phase-changing perfluorocarbon single emulsions, in which perfluorocarbon nanodroplets can be vaporized from liquid nanodroplets to gas microbubbles by ultrasound exposure[42,49]. It has been shown that small nanodroplets require a higher energy to be vaporized because the Laplace pressure increases, causing the effective boiling point of the perfluorocarbon in the nanodroplets to increase[42,49]. To test this hypothesis, we developed two larger nanodroplets (with average diameters of ~450 and ~800 nm) aiming to decrease the Laplace pressure and consequently reduce the effective boiling point of the perfluorocarbon nanodroplets. We used perfluoropentane because its boiling point is close to room temperature (28 °C), which is at the boundary of becoming unstable and more susceptible to the increment of size. Figure 2h confirms that among the perfluoropentane nanodroplets, greater increase in sizes (that is, reduced stability) of the larger nanodroplets were observed compared to the small nanodroplets upon incubation for 14 days (103 ± 18%, 139 ± 18% and 142 ± 20% for 250, 450 and 800 nm droplets, respectively). Overall, these results suggest that choosing a perfluorocarbon liquid with a low vapour pressure or reducing the size of the nanodroplets can improve the stability for longitudinal imaging.

## Optimization of UHF-RF-acoustic signals

To determine the optimum saline concentration, nanodroplets encapsulated with four concentrations of NaCl(aq.) solutions (25, 20, 15 and 10 wt%) at $2\times10^9$ nanodroplets ml$^{-1}$ were assessed in a tube phantom (Fig. 3a–d and Supplementary Fig. 3). As a control, another tube was filled with physiological saline (0.9 wt% NaCl) to mimic UHF-RF-acoustic background signals of tissue. As expected, the UHF-RF-acoustic signal of the nanodroplets increases linearly with the saline concentration ($R^2=0.99$), confirming the successful encapsulation of saline within these nanodroplets. We then selected the optimum nanodroplets with 25 wt% saline and assessed the correlation between UHF-RF-acoustic signals and nanodroplet concentrations. Figure 3b shows that the UHF-RF-acoustic signals highly correlate with the concentration of the nanodroplets ($R^2=0.99$). In addition, $2\times10^8$ nanodroplets ml$^{-1}$ (25 wt%) and physiological saline (no droplets) produce comparable UHF-RF-acoustic signals, providing an estimated detection limit of these nanodroplets in tissue.

We compared the performance of our nanodroplets with other nanoparticles operating in the RF range but at higher frequencies (microwave, >1 GHz)[24,49] using a similar tube phantom (Fig. 2a).

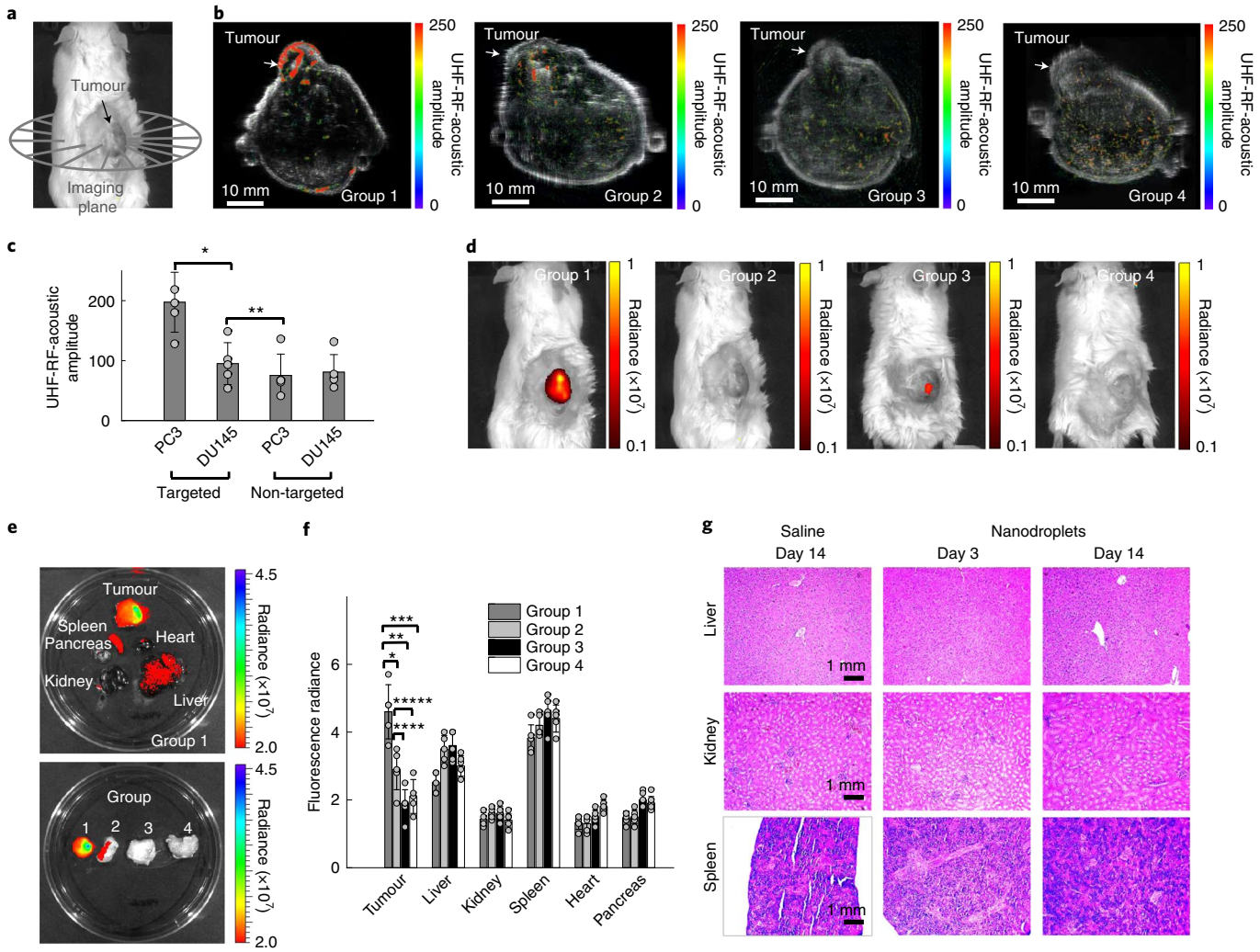


**Fig. 5 | In vivo UHF-RF-acoustic molecular imaging using targeted nanodroplets. a**, Configuration of the tomographic mouse imaging. **b**, In vivo UHF-RF-acoustic imaging with subcutaneous GRPR$^+$ tumours (PC3) using targeted nanodroplets (group 1, $n=5$), GRPR$^-$ tumours (DU145) using targeted nanodroplets (group 2, $n=5$), PC3 tumours using non-targeted nanodroplets (group 3, $n=5$) and DU145 tumours using non-targeted nanodroplets (group 4, $n=5$). **c**, Comparison of UHF-RF-acoustic signal amplitude in the tumour region with targeted and non-targeted nanodroplets, showing the strongest signals from the targeted nanodroplets with PC3 tumours (*$P=0.007$; **$P=0.404$). Data are presented as mean values ± s.d. ($n=5$). **d**, Epifluorescence imaging of mice in groups 1–4 at 48 h postinjection, showing the strongest ICG fluorescence signals from a PC3 tumour-bearing mouse with GRPR-targeted nanodroplets. The scanning area is 66 mm × 50 mm. **e**, Fluorescence imaging (top) of harvested main organs and tumour from one mouse in group 1, showing that the nanodroplets mainly accumulate at the tumour and the spleen. Fluorescence imaging (bottom) of the harvested tumours from one mouse from each group, showing the strongest signal from the mouse in group 1, demonstrating their highest targeting specificity and efficiency. **f**, ICG fluorescence signals from the major organs and tumours from the four groups of mice, indicating that the nanodroplets mainly accumulate at the tumour and the spleen, but only GRPR-targeted nanodroplets show the highest binding specificity at the tumour site (*$P=0.006$; **$P=0.0005$; ***$P=0.0007$; ****$P=0.017$; *****$P=0.051$). Data are presented as mean values ± s.d. ($n=5$). **g**, Immunohistochemical tissue sections of liver, kidney and spleen from mice with non-targeted nanodroplet or saline injections (100 µl, $1\times10^{11}$ nanodroplets ml$^{-1}$) for 2 weeks, stained with haematoxylin and eosin and Perls Prussian blue. There was no noticeable tissue damage from the intravenous nanodroplet injections.

Four tubes were filled with nanodroplets (25 wt% saline, $1\times10^9$ nanodroplets ml$^{-1}$), one with gold nanoparticles (20 nm in diameter, $5\times10^{11}$ nanoparticles ml$^{-1}$) and one with $Fe_3O_4$ nanoparticles (100 nm in diameter, $5\times10^{11}$ nanoparticles ml$^{-1}$). Figure 3d shows the UHF-RF-acoustic imaging of these tube phantoms (middle panel) and the statistical comparison of their quantified signals (right panel). Although the gold and $Fe_3O_4$ nanoparticles were 500 times more concentrated than our nanodroplet solution, the UHF-RF-acoustic signals from our nanodroplets were statistically higher. We quantified the signal amplitude from the images and normalized it by the nanoparticle concentration. The result shows the UHF-RF-acoustic signal of our nanodroplets is 2,500 ± 30 and 1,600 ± 35 times higher than the signals of gold and $Fe_3O_4$ nanoparticles, respectively.

One of the key strengths of UHF-RF-acoustic molecular imaging is its potential in deep tissue imaging applications. To demonstrate this capability, we built two bovine tissue phantoms. One phantom contains six 3-mm-diameter inclusions at different depths beneath the surface (Fig. 3e). Inclusions located 5 cm deep in tissue were detectable. For demonstration in even deeper tissue, another bovine tissue phantom (~9 cm × 9 cm) was developed, where a hole (2.2 cm in diameter) was drilled in the tissue, and tightly fitted with a Stanford logo-shaped agar gel phantom (Fig. 3f). The logo contains spatial features as small as ~1–2 mm (the branches of the redwood

tree), with which we demonstrated deep-tissue imaging of 25 wt% saline nanodroplets at 7 cm beneath the surface, visualizing the 1 mm features (Fig. 3f and Supplementary Fig. 5).

### In vivo UHF-RF-acoustic molecular Imaging

Gastrin-releasing peptide receptor (GRPR) is our target of interest for in vivo molecular imaging, as it is a biomarker overexpressed in many cancers, including prostate, breast, colon and lung cancers[25]. Targeting of GRPR was achieved by coupling an anti-GRPR antibody to the saline nanodroplet surface; a maleimide–indocyanine green (ICG) dye was also linked to the surface to allow fluorescence imaging for assessing targeting specificity in vitro and in vivo (see 'Anti-GRPR antibody and ICG dye conjugation on nanodroplets' in Supplementary Information).

We first confirmed GRPR expression in a panel of prostate cancer cell lines using Western blot analysis (Fig. 4b). High GRPR-expressing PC3 cells ($GRPR^+$) and low GRPR-expressing DU145 cells ($GRPR^-$) were chosen as our positive and negative controls, respectively. Before the in vitro binding studies, the cytotoxicity of the targeted nanodroplets on prostate cancer cells was evaluated with a Presto Blue cell viability assay. Our results show no obvious reduction in cell viability when cells were incubated with up to $1\times10^{11}$ nanodroplets $ml^{-1}$ for 24 h, while a reduction to 70% was observed with $3\times10^{11}$ nanodroplets $ml^{-1}$ (Fig. 4c).

To evaluate the GRPR-targeting specificity of our nanodroplets, both $GRPR^+$ and $GRPR^-$ cell lines were incubated with either targeted (GRPR) or non-targeted (polyethylene glycol (PEG)) nanodroplets ($1\times10^8$ nanodroplets for $1\times10^5$ cells) for 2 h. PC3 cells show 2.5-fold higher ICG fluorescence signals when incubated with GRPR-targeted nanodroplets compared with non-targeted nanodroplets (Supplementary Fig. 8). As expected, the negative control cell line DU145 shows negligible fluorescence signals when incubated with either targeted or non-targeted nanodroplets (Fig. 4d and Supplementary Fig. 8). To further confirm molecular specificity, we performed a blocking study in which PC3 cells were preincubated with anti-GRPR antibody in excess for 30 min prior to incubation with GRPR-targeted saline nanodroplets. We found that preincubation with anti-GRPR antibody significantly decreased the binding of the nanodroplets, as shown by the lower ICG fluorescence signals compared with those without blocking (Fig. 4d). Overall, our in vitro blocking tests (Supplementary Fig. 8) and competitive binding experiments (Supplementary Fig. 9) confirm the specificity of our GRPR-targeted saline nanodroplets.

Six-week-old male NOD-SCID-IL2R$\gamma^{null}$ (NSG) tumour-bearing mice were randomized into four groups ($n=5$ per group): two groups of mice were subcutaneously implanted with PC3 cancer cells (groups 1 and 3) and two groups were implanted with DU145 cells (groups 2 and 4) at the mid-dorsal region of each mouse (see 'Animal studies' in Supplementary Information). In addition to UHF-RF-acoustic imaging, the pharmacokinetics, in vivo targeting specificity and biodistribution of ICG-labelled nanodroplets were also evaluated by fluorescence imaging using ICG nanodroplets (Supplementary Figs. 13–15). Each tumour-bearing mouse was injected with 100 µl of nanodroplet solution via the tail vein ($1\times10^{11}$ nanodroplets $ml^{-1}$); groups 1 and 2 were injected with GRPR-targeted nanodroplets, whereas groups 3 and 4 were injected with non-targeted nanodroplets. Forty-eight hours after injection, UHF-RF-acoustic and fluorescence imaging of all mice were performed. A representative mouse image from each group is shown in Fig. 5b; these reveal visibly higher UHF-RF-acoustic signals from the PC3 tumour with GRPR-targeted nanodroplets (group 1), compared with signals from tumours in groups 2–4, indicating the in vivo GRPR specificity of our targeted nanodroplets. Quantitative analyses (Fig. 5c) of the UHF-RF-acoustic signals also show significantly higher signals in group 1 ($2.4\pm0.3$-fold) than in groups 2–4. Immediately after UHF-RF-acoustic imaging, whole-body fluorescence imaging was performed to confirm the successful delivery and targeting of the ICG-labelled nanodroplets (Fig. 5d). The higher ICG fluorescence signals in the tumours of group 1 compared with groups 2–4 further confirmed the specificity of the targeted nanodroplets to GRPR-expressing tumours, which corroborated our UHF-RF-acoustic imaging results (Fig. 5b).

Immediately following in vivo imaging, we excised the key organs (heart, liver, kidney, spleen, pancreas) and tumours to quantitatively assess the biodistribution of the nanodroplets (Fig. 5e,f). Figure 5f shows that the fluorescence signals in the tumours of group 1 were significantly higher than the rest of the groups ($1.6\pm0.4$-fold, $2.4\pm0.6$-fold and $2.2\pm0.6$-fold higher than groups 2, 3 and 4, respectively). In addition, fluorescence signals in the tumours of groups 3 and 4 were relatively low but detectable. This low level of fluorescence signal could be due to non-specific uptake and/or the enhanced permeability and retention effects of the non-targeted nanodroplets[50]. The slightly higher fluorescence signals in the tumours from group 2 with targeted nanodroplets compared with that from non-targeted nanodroplets in groups 3 and 4 ($1.5\pm0.4$-fold and$1.4\pm0.4$-fold, respectively) is probably due to minimal GRPR expression of the DU145 cells, as observed in our in vitro evaluation (Fig. 4b). Moreover, fluorescence quantification shows that in addition to tumour uptake, both targeted and non-targeted nanodroplets accumulated in the spleen and liver while negligible signals were detected in the other organs due to the elimination by the reticuloendothelial system (Fig. 5f). Pilot toxicity studies on healthy male mice show no adverse effect on the total blood count, relative to clinical pathology reference ranges (Supplementary Table 1), or visible damage to any tissue of key organs by histology (Fig. 5g) after 14 days of intravenous nanodroplet injection ($1\times10^{10}$ nanodroplets).

## Conclusions

UHF-RF-acoustic imaging is a low-cost, portable and non-ionizing imaging technique for deep-tissue imaging. It provides imaging penetration of up to ~10 cm with ultrasound resolution in tissue. The main obstacle to extending UHF-RF-acoustic imaging to molecular imaging applications is the lack of imaging contrast agents. In this study, we developed an approach to produce stable, all-liquid UHF-RF-acoustic contrast agents using saline and non-toxic surfactants. We show that our contrast agents can produce 1,600 times higher UHF-RF-acoustic signals than concentration-matched $Fe_3O_4$ nanoparticles. Finally, we demonstrated in vivo UHF-RF-acoustic molecular imaging by using the targeted nanodroplets in a prostate cancer xenograft mouse model expressing GRPR. We expect these findings will accelerate the development of UHF-RF-acoustic molecular imaging for other cell surface targets and various disease states. In addition, the finding that perfluorocarbon liquid can stabilize high-ionic liquids into stable nanodroplets will also benefit the development of nanocarriers to deliver high-ionic prodrugs for disease treatment.

## Online content

Any methods, additional references, Nature Research reporting summaries, source data, extended data, supplementary information, acknowledgements, peer review information; details of author contributions and competing interests; and statements of data and code availability are available at https://doi.org/10.1038/s41565-021-00869-5.

Received: 4 July 2019; Accepted: 28 January 2021;
Published online: 29 March 2021

## References

1. Gambhir, S. S., Ge, T. J., Vermesh, O. & Spitler, R. Toward achieving precision health. *Sci. Transl. Med.* **10**, eaao3612 (2018).

2. Hamilton, W., Walter, F. M., Rubin, G. & Neal, R. D. Improving early diagnosis of symptomatic cancer. *Nat. Rev. Clin. Oncol.* **13**, 740–749 (2016).
3. Gambhir, S. S. Molecular imaging of cancer with positron emission tomography. *Nat. Rev. Cancer* **2**, 683–693 (2002).
4. Weissleder, R. Molecular imaging in cancer. *Science* **312**, 1168–1171 (2006).
5. Weissleder, R. & Mahmood, U. Molecular imaging. *Radiology* **219**, 316–333 (2001).
6. Hussain, T. & Nguyen, Q. T. Molecular imaging for cancer diagnosis and surgery. *Adv. Drug Deliv. Rev.* **66**, 90–100 (2014).
7. Willmann, J. K., van Bruggen, N., Dinkelborg, L. M. & Gambhir, S. S. Molecular imaging in drug development. *Nat. Rev. Drug Discov.* **7**, 591–607 (2008).
8. Pysz, M. A., Gambhir, S. S. & Willmann, J. K. Molecular imaging: current status and emerging strategies. *Clin. Radiol.* **65**, 500–516 (2010).
9. Lin, E. C. Radiation risk from medical imaging. *Mayo Clin. Proc.* **85**, 1142–1146 (2010).
10. James, M. L. & Gambhir, S. S. A molecular imaging primer: modalities, imaging agents, and applications. *Physiological Rev.* **92**, 897–965 (2012).
11. Loskutova, K., Grishenkov, D. & Ghorbani, M. Review on acoustic droplet vaporization in ultrasound diagnostics and therapeutics. *BioMed. Res. Int.* **2019**, 9480193 (2019).
12. Jokerst, J. V. & Gambhir, S. S. Molecular imaging with theranostic nanoparticles. *Acc. Chem. Res.* **44**, 1050–1060 (2011).
13. Weber, J., Beard, P. C. & Bohndiek, S. E. Contrast agents for molecular photoacoustic imaging. *Nat. Methods* **13**, 639–650 (2016).
14. Bowen, T. in *Proc. 1981 IEEE Ultrasonics Symposium* 817–822 (IEEE, 1981).
15. Kruger, R. A. et al. Thermoacoustic CT with radio waves: a medical imaging paradigm. *Radiology* **211**, 275–278 (1999).
16. Ku, G. et al. Thermoacoustic and photoacoustic tomography of thick biological tissues toward breast imaging. *Technol. Cancer Res. Treat.* **4**, 559–565 (2005).
17. Kruger, R. A., Reinecke, D. R. & Kruger, G. A. Thermoacoustic computed tomography—technical considerations. *Med. Phys.* **26**, 1832–1837 (1999).
18. Wen, L. W., Yang, S. H., Zhong, J. P., Zhou, Q. & Xing, D. Thermoacoustic imaging and therapy guidance based on ultra-short pulsed microwave pumped thermoelastic effect induced with superparamagnetic iron oxide nanoparticles. *Theranostics* **7**, 1976–1989 (2017).
19. Kruger, R. A. et al. Breast cancer in vivo: contrast enhancement with thermoacoustic CT at 434 MHz—feasibility study. *Radiology* **216**, 279–283 (2000).
20. Omar, M., Kellnberger, S., Sergiadis, G., Razansky, D. & Ntziachristos, V. Near-field thermoacoustic imaging with transmission line pulsers. *Med. Phys.* **39**, 4460–4466 (2012).
21. Laqua, D., Just, T. & Husar, P. in *Proc. 2010 Annual International Conference of the IEEE Engineering in Medicine and Biology Society* 1437–1440 (IEEE, 2010).
22. Ogunlade, O. & Beard, P. Exogenous contrast agents for thermoacoustic imaging: an investigation into the underlying sources of contrast. *Med. Phys.* **42**, 170–181 (2016).
23. Byrd, D., Hanson, G.W. & Patch, S.K. in *Proc. SPIE 7564, Photons Plus Ultrasound: Imaging and Sensing 2010*, 756417 (SPIE, 2010).
24. Wu, D., Huang, L., Jiang, M. S. & Jiang, H. Contrast agents for photoacoustic and thermoacoustic imaging: a review. *Int. J. Mol. Sci.* **15**, 23616 (2014).
25. Nie, L., Ou, Z., Yang, S. & Xing, D. Thermoacoustic molecular tomography with magnetic nanoparticle contrast agents for targeted tumor detection. *Med. Phys.* **37**, 4193–4200 (2010).
26. Tamarov, K. et al. Electrolytic conductivity-related radiofrequency heating of aqueous suspensions of nanoparticles for biomedicine. *Phys. Chem. Chem. Phys.* **19**, 11510–11517 (2017).
27. Weast, R.C. *CRC Handbook of Chemistry and Physics* 70th edn (CRC Press, 1989).
28. Wolf, A. V. *Aqueous Solutions and Body Fluids* (Harper & Row, 1966).
29. Engel, R. H., Riggi, S. J. & Fahrenbach, M. J. Insulin: intestinal absorption as water-in-oil-in-water emulsions. *Nature* **219**, 856–857 (1968).
30. Gresham, P. A., Barnett, M., Smith, S. V. & Schneider, R. Use of a sustained-release multiple emulsion to extend the period of radioprotection conferred by cysteamine. *Nature* **234**, 149 (1971).
31. Garti, N. & Bisperink, C. Double emulsions: progress and applications. *Curr. Opin. Colloid Interface Sci.* **3**, 657–667 (1998).
32. Muschiolik, G. Multiple emulsions for food use. *Curr. Opin. Colloid Interface Sci.* **12**, 213–220 (2007).
33. Chong, D. et al. Advances in fabricating double-emulsion droplets and their biomedical applications. *Microfluidics Nanofluidics* **19**, 1071–1090 (2015).
34. Chen, L. et al. Photoresponsive monodisperse cholesteric liquid crystalline microshells for tunable omnidirectional lasing enabled by a visible light-driven chiral molecular switch. *Adv. Optical Mater.* **2**, 845–848 (2014).
35. Mezzenga, R., Folmer, B. M. & Hughes, E. Design of double emulsions by osmotic pressure tailoring. *Langmuir* **20**, 3574–3582 (2004).
36. Wen, L. & Papadopoulos, K. D. Effects of osmotic pressure on water transport in W1/O/W2 emulsions. *J. Colloid Interface Sci.* **235**, 398–404 (2001).
37. Atzberger, P. J. & Kramer, P. R. Theoretical framework for microscopic osmotic phenomena. *Phys. Rev. E Stat. Nonlin. Soft Matter Phys.* **75**, 061125 (2007).
38. Freire, M. G., Dias, A. M. A., Coelho, M. A. Z., Coutinho, J. A. P. & Marrucho, I. M. Aging mechanisms of perfluorocarbon emulsions using image analysis. *J. Colloid Interface Sci.* **286**, 224–232 (2005).
39. Hilder, M. H. The solubility of water in edible oils and fats. *J. Am. Oil Chem. Soc.* **45**, 703–707 (1968).
40. Freire, M. G., Gomes, L., Santos, L. M., Marrucho, I. M. & Coutinho, J. A. Water solubility in linear fluoroalkanes used in blood substitute formulations. *J. Phys. Chem. B* **110**, 22923–22929 (2006).
41. Rotariu, G., Fraga, D. & Hildebrand, J. The solubility of water in normal perfluoroheptane. *J. Am. Chem. Soc.* **75**, 6357–6357 (1953).
42. Shpak, O. et al. Acoustic droplet vaporization is initiated by superharmonic focusing. *Proc. Natl Acad. Sci. USA* **111**, 1697–1702 (2014).
43. Vernikouskaya, I., Pochert, A., Lindén, M. & Rasche, V. Quantitative $^{19}$F MRI of perfluoro-15-crown-5-ether using uniformity correction of the spin excitation and signal reception. *Magn. Reson. Mater. Phys., Biol. Med.* **32**, 25–36 (2019).
44. Tran, T. D. et al. Clinical applications of perfluorocarbon nanoparticles for molecular imaging and targeted therapeutics. *Int. J. Nanomed.* **2**, 515–526 (2007).
45. Joseph, G. M. & Noah, W. Poloxamer 188 (P188) as a membrane resealing reagent in biomedical applications. *Recent Pat. Biotechnol.* **6**, 200–211 (2012).
46. Lifshitz, I. M. & Slyozov, V. V. The kinetics of precipitation from supersaturated solid solutions. *J. Phys. Chem. Solids* **19**, 35–50 (1961).
47. Sakai, T., Kamogawa, K., Nishiyama, K., Sakai, H. & Abe, M. Molecular diffusion of oil/water emulsions in surfactant-free conditions. *Langmuir* **18**, 1985–1990 (2002).
48. Doinikov, A. A., Sheeran, P. S., Bouakaz, A. & Dayton, P. A. Vaporization dynamics of volatile perfluorocarbon droplets: a theoretical model and in vitro validation. *Med. Phys.* **41**, 102901 (2014).
49. Pitt, W. G., Singh, R. N., Perez, K. X., Husseini, G. A. & Jack, D. R. Phase transitions of perfluorocarbon nanoemulsion induced with ultrasound: a mathematical model. *Ultrason. Sonochem.* **21**, 879–891 (2014).
50. Cornelio, D. B., Roesler, R. & Schwartsmann, G. Gastrin-releasing peptide receptor as a molecular target in experimental anticancer therapy. *Ann. Oncol.* **18**, 1457–1466 (2007).

**Reporting Summary.** Further information on research design is available in the Nature Research Reporting Summary linked to this article.

## Data availability

The data that support the plots within this paper and other findings of this study are available from the corresponding author upon reasonable request.

## Acknowledgements

This work was supported in part by grants from NCI CCNE-TD U54 CA199075-04 (S.S.G.), The Canary Foundation (S.S.G.), The Sir Peter Michael Foundation (S.S.G.), Stanford's Catalyst for Collaborative Solutions (J.D. and S.S.G.), Google Faculty Research Award (Y.-S.C.), The Jump ARCHES endowment through the Health Care Engineering Systems Center (Y.-S.C.), and NIGMS 1R21GM139022-01 (Y.Z.). The authors acknowledge the Stanford Center for Innovation in In Vivo Imaging (SCI$^3$) for assistance with animal imaging and C. Chan for providing insightful discussions. This paper is dedicated to the memory of Dr Sanjiv Sam Gambhir.

## Author contributions

S.S.G. conceived the original idea. Y.-S.C. and S.S.G. designed the experiments. Y.-S.C. developed the contrast agents and performed the in vitro and in vivo imaging. C.B., A.Z. and F.A. assisted in the in vivo experiments. Y.-S.C., Y.Z. and H.W. performed the theoretical study. D.-H.C. contributed to cryo-electron microscopy. C.B., A.Z., E.-C.H., F.A., T.S. and J.D. contributed to the discussion of the data and experimental results. Y.-S.C. and S.S.G. drafted the manuscript and all authors contributed to the writing of the manuscript. S.S.G. supervised the entire study.

## Competing interests

S.S.G. declared competing financial interests with Endra Inc and Visualsonics Inc.

## Additional information

**Supplementary information** The online version contains supplementary material available at https://doi.org/10.1038/s41565-021-00869-5.

**Correspondence and requests for materials** should be addressed to Y.-S.C.

**Peer review information** *Nature Nanotechnology* thanks F. Kiessling, N. van den Berg and M. Tang for their contribution to the peer review of this work.

**Reprints and permissions information** is available at www.nature.com/reprints.

nature research

Corresponding author(s): Yun-Sheng Chen

Last updated by author(s): 2/1/2021

# Reporting Summary

Nature Research wishes to improve the reproducibility of the work that we publish. This form provides structure for consistency and transparency in reporting. For further information on Nature Research policies, see our Editorial Policies and the Editorial Policy Checklist.

## Statistics

For all statistical analyses, confirm that the following items are present in the figure legend, table legend, main text, or Methods section.

| n/a | Confirmed | |
|---|---|---|
| ☐ | ☒ | The exact sample size (*n*) for each experimental group/condition, given as a discrete number and unit of measurement |
| ☐ | ☒ | A statement on whether measurements were taken from distinct samples or whether the same sample was measured repeatedly |
| ☐ | ☒ | The statistical test(s) used AND whether they are one- or two-sided<br>*Only common tests should be described solely by name; describe more complex techniques in the Methods section.* |
| ☐ | ☒ | A description of all covariates tested |
| ☐ | ☒ | A description of any assumptions or corrections, such as tests of normality and adjustment for multiple comparisons |
| ☐ | ☒ | A full description of the statistical parameters including central tendency (e.g. means) or other basic estimates (e.g. regression coefficient) AND variation (e.g. standard deviation) or associated estimates of uncertainty (e.g. confidence intervals) |
| ☐ | ☒ | For null hypothesis testing, the test statistic (e.g. *F*, *t*, *r*) with confidence intervals, effect sizes, degrees of freedom and *P* value noted<br>*Give P values as exact values whenever suitable.* |
| ☒ | ☐ | For Bayesian analysis, information on the choice of priors and Markov chain Monte Carlo settings |
| ☒ | ☐ | For hierarchical and complex designs, identification of the appropriate level for tests and full reporting of outcomes |
| ☒ | ☐ | Estimates of effect sizes (e.g. Cohen's *d*, Pearson's *r*), indicating how they were calculated |

*Our web collection on statistics for biologists contains articles on many of the points above.*

## Software and code

Policy information about availability of computer code

| | |
|---|---|
| Data collection | IVIS fluorescence images were collected using Living Image 4.5<br>Dynamic light scattering data was collected using Zetasizer Nano ZS Software<br>UHF-RF-acoustic images were collected using specialized software from ENDRA<br>Ultrasound images were collected using VisualSonics Vevo LZER data collection software<br>UV-Vis data was collected using Biotek Gen5 software |
| Data analysis | COMSOL Multiphysics, ImageJ, Amira, OriginPro, Living Image, and Matlab. |

For manuscripts utilizing custom algorithms or software that are central to the research but not yet described in published literature, software must be made available to editors and reviewers. We strongly encourage code deposition in a community repository (e.g. GitHub). See the Nature Research guidelines for submitting code & software for further information.

## Data

Policy information about availability of data

All manuscripts must include a data availability statement. This statement should provide the following information, where applicable:

- Accession codes, unique identifiers, or web links for publicly available datasets
- A list of figures that have associated raw data
- A description of any restrictions on data availability

The data that support the findings of this study are available from the corresponding authors upon reasonable request.

# Field-specific reporting

Please select the one below that is the best fit for your research. If you are not sure, read the appropriate sections before making your selection.

☒ Life sciences ☐ Behavioural & social sciences ☐ Ecological, evolutionary & environmental sciences

For a reference copy of the document with all sections, see nature.com/documents/nr-reporting-summary-flat.pdf

# Life sciences study design

All studies must disclose on these points even when the disclosure is negative.

| | |
|---|---|
| Sample size | An unpaired t-test was used to determine the significance between groups. Five mice were used in each group, and there were four groups in total. The sample size was determined using "resource equation" based on the law of diminishing returns (J Pharmacol Pharmacother 2013, 4(4): 303–306.). A value "E" was calculated, which was 16 in our experiment. Based on the literature, the value "E" above 10 is considered adequate. |
| Data exclusions | No data were excluded. |
| Replication | All attempts at replication were successful. |
| Randomization | Animals were randomly assigned and the samples were randomly distributed into experimental groups. |
| Blinding | The investigators were not blinded to the animal experiments, yet, we acquired the imaging data using a computer controlled instrument with the same setting through the entire experiment to prevent bias. The image processing parameters and data analysis procedures were kept the same for all samples. |

# Reporting for specific materials, systems and methods

We require information from authors about some types of materials, experimental systems and methods used in many studies. Here, indicate whether each material, system or method listed is relevant to your study. If you are not sure if a list item applies to your research, read the appropriate section before selecting a response.

## Materials & experimental systems

| n/a | Involved in the study |
|---|---|
| ☐ | ☒ Antibodies |
| ☐ | ☒ Eukaryotic cell lines |
| ☒ | ☐ Palaeontology and archaeology |
| ☐ | ☒ Animals and other organisms |
| ☒ | ☐ Human research participants |
| ☒ | ☐ Clinical data |
| ☒ | ☐ Dual use research of concern |

## Methods

| n/a | Involved in the study |
|---|---|
| ☒ | ☐ ChIP-seq |
| ☒ | ☐ Flow cytometry |
| ☒ | ☐ MRI-based neuroimaging |

## Antibodies

| | |
|---|---|
| Antibodies used | Glyceraldehyde 3-anti-gastrin-releasing peptide receptor antibody (AbCam), phosphate dehydrogenase (GAPDH) loading control monoclonal antibody (Thermo Fisher Scientific), anti-GRPR antibody (AbCam) |
| Validation | All commercial antibodies are validated by the manufacturers. |

## Eukaryotic cell lines

Policy information about cell lines

| | |
|---|---|
| Cell line source(s) | ARCap cell line was from Dr. Stoyanova's lab. The rest cell lines are purchased from ATCC. |
| Authentication | Cell lines obtained from ATCC were used as is without further authentication; ARCap was autheticated by short tandem repeat(STR)DNA profile analysis. |
| Mycoplasma contamination | All cell lines are tested by MycoAlert Mycoplasma Detection Kit monthly and right before experiments. |
| Commonly misidentified lines (See ICLAC register) | None |

## Animals and other organisms

Policy information about studies involving animals; ARRIVE guidelines recommended for reporting animal research

| | |
|---|---|
| Laboratory animals | Healthy male NSG mice and Male nu/nu mice at age 6 weeks were used in the study. All animal experiments were performed in compliance with the Guidelines for the Care and Use of Research Animals established by the Stanford University Animal Studies Committee, under the protocol APLAC-13024. |
| Wild animals | No wild animals |
| Field-collected samples | No field-collected samples |
| Ethics oversight | Stanford Center for Biomedical Ethics |

Note that full information on the approval of the study protocol must also be provided in the manuscript.